International Journal of Heat and Mass Transfer 52 (2009) 4997–5004

Contents lists available at ScienceDirect

International Journal of Heat and Mass Transfer

journal homepage: www.elsevier.com/locate/ijhmt

Particle–gas reacting flow under concentrated solar irradiation

G. Maag [a], W. Lipiński [b], A. Steinfeld [a,c,*]

[a] Department of Mechanical and Process Engineering, ETH Zurich, 8092 Zurich, Switzerland
[b] Department of Mechanical Engineering, University of Minnesota, Minneapolis, MN 55455, USA
[c] Solar Technology Laboratory, Paul Scherrer Institute, 5232 Villigen, Switzerland

ARTICLE INFO

Article history:
Received 23 July 2008
Received in revised form 6 February 2009
Accepted 27 February 2009
Available online 25 June 2009

Keywords:
Radiation
Transient
Heterogeneous
Hydrogen
Carbon
Methane
Thermochemical
Solar energy

ABSTRACT

A transient heat transfer model is developed for a reacting flow of CH_4 laden with carbon particles directly exposed to concentrated solar radiation and undergoing thermal decomposition into carbon and hydrogen. The unsteady mass and energy conservation equations, coupling convective heat and mass transfer, radiative heat transfer, and chemical kinetics for a two-phase solid–gas flow, are formulated and solved numerically for both phases by Monte Carlo and finite volume methods using the explicit Euler time integration scheme. Parametric study is performed with respect to the initial particle diameter, volume fraction, gas composition, and velocity. Validation is accomplished by comparing temperatures and reaction extent with those measured experimentally using a particle-flow solar reactor prototype subjected to concentrated solar radiation. Smaller particles and/or high volume fractions increase the optical thickness of the medium, its radiative absorption and extinction coefficients, and lead to higher steady-state temperatures, reaction rates, and consequently, higher extent of chemical conversion.

1. Introduction

Hybrid solar-fossil thermochemical processes make use of concentrated solar radiation as the source of high-temperature process heat [1–3]. Industrially relevant examples include the thermal gasification of carbonaceous materials [4–6], the thermal cracking of natural gas [7–9], the thermal reforming of natural gas [10–12], and the carbothermic reduction of metal oxides [13,14], for producing synthetic fluid fuels with upgraded calorific value. These hybrid solar-driven processes offer viable and efficient routes for fossil fuel decarbonization and CO_2 avoidance, and further create a transition path towards solar hydrogen. The solar chemical reactors for effecting these high-temperature gas–solid transformations usually feature cavities containing directly-irradiated reacting particles, to provide efficient energy transfer to the reaction site, bypassing the limitations imposed by indirect heat transfer through reactor walls [15]. Chemical reactors based on the concept of direct irradiation require matching the rate of radiative heat transfer to the rate of the chemical reaction. Modeling such an interaction is needed for anticipating the consequences of a given design decision on the reactor's performance, and for optimizing the reactor design for maximum solar-to-chemical energy conversion efficiency.

Previous pertinent studies of transient radiative heat transfer in solar-driven solid–gas reactions include models for suspensions of coal particles undergoing steam gasification [16,17], packed beds of $CaCO_3$ particles undergoing thermal decomposition [18], and of ZnO particles undergoing thermal and carbothermal reduction [19–21]. Steady-state radiative transfer analysis of solar reactions was applied for the thermal decomposition of CH_4 [22], solar combined CH_4-reforming and ZnO-reduction [23], gasification of coal [24,25] and petroleum coke [26]. Examples of analyses of non-solar reactors involving heterogeneous chemical systems include coal gasification in packed beds [27], fluidized beds [28], and entrained gasifiers [29], combustion in porous burners [30,31], and biomass pyrolysis [32]. Further examples of radiative heat transfer analyses include studies on direct absorption of concentrated solar radiation by particle suspensions [33–35].

In the present paper, a transient radiation-convection heat transfer model is developed for a reactive two-phase system composed of a CH_4 flow laden with C particles, whose thermal and optical properties vary as the decomposition reaction progresses. Temperatures and gas composition are computed for boundary and initial conditions (initial/inlet particle diameter, particle volume fraction, gas phase composition, inlet gas velocity, and incident solar radiative flux) anticipated for a solar reactor. Emphasis is placed on the detailed investigation of the wavelength and directional depended radiative exchange within the particle suspension.

---

* Corresponding author. Address: Department of Mechanical and Process Engineering, ETH Zurich, 8092 Zurich, Switzerland. Tel.: +41 44 6327929; fax: +41 44 6321065.
E-mail address: aldo.steinfeld@eth.ch (A. Steinfeld).

0017-9310/$ - see front matter © 2009 Elsevier Ltd. All rights reserved.
doi:10.1016/j.ijheatmasstransfer.2009.02.049

Nomenclature

A	absorbed cumulative fraction of incident radiation
Bi	Biot number
$\bar{c}_p$	specific heat at constant pressure (J mol^{-1} K^{-1})
d	particle diameter (m)
E_a	activation energy (J mol^{-1})
f	particle-number based size distribution function (m^{-4})
f_v	particle volume fraction
h	heat transfer coefficient (W m^{-2} K^{-1})
$\bar{h}$	specific enthalpy (J mol^{-1})
I_λ	spectral radiation intensity (W m^{-3} sr^{-1})
k	thermal conductivity (W m^{-1} K^{-1})
k_0	frequency factor (s^{-1})
$\hat{\mathbf{k}}$	unit vector of the z-Cartesian coordinate
L	slab thickness (m)
$\overline{M}$	molar mass (kg mol^{-1})
m	complex refractive index, $m = n - ik$
N_{rays}	total number of stochastic rays in the simulation
$\dot{n}$	molar flux (mol s^{-1} m^{-2})
p	pressure (Pa)
Q	efficiency factor
$\dot{q}$	heat flux (W m^{-2})
$\overline{R}$	universal gas constant (8.314 J mol^{-1} K^{-1})
$\bar{r}$	reaction rate (mol s^{-1} mol(C)$^{-1}$)
S_λ	spectral radiation source function (W m^{-3} sr^{-1})
s	path length (m)
$\hat{\mathbf{s}}$	unit vector into a given direction
T	temperature (K)
t	time (s)
V	volume (m^3)
X_{CH_4}	extent of methane conversion
z	Cartesian coordinate (m)
$\bar{x}$	mole fraction

Greek symbols

β	extinction coefficient (m^{-1})
Γ	number of particles per unit volume (m^{-3})
$\dot{\gamma}$	particle number flux (m^{-2} s^{-1})
δ	Kronecker delta function
ε	emissivity
η	wavenumber (m^{-1})
κ	absorption coefficient (m^{-1})
λ	wavelength (m)
ν	stoichiometric coefficient
ρ	density (kg m^{-3}); mass concentration (kg m^{-3})
$\bar{\rho}$	molar concentration (mol m^{-3})
σ	Stefan–Boltzmann constant, $\sigma = 5.6704 \times 10^{-8}$ W m^{-2} K^{-4})
σ_{sca}	scattering coefficient (m^{-1})
Φ	scattering phase function

Other symbols

∇	Nabla operator
$\mathscr{R}$	random number from a uniform distribution (0, 1)

Subscripts

abs	absorption
Ar	argon
b	blackbody
C	carbon
CH_4	methane
c	conduction
e	external source of radiation
exp	experimental
ext	extinction
g	gas phase
H_2	hydrogen
i	incoming
num	numerical
outlet	flow outlet
P	Planck mean
p	particles; solid phase
r	radiative
ray	generic ray in MC
sca	scattering
surr	surroundings
λ	spectral
0	initial/inlet
32	Sauter-mean

Abbreviations

CCD	charge-coupled device
GC	gas chromatography
IR	infrared
MC	Monte Carlo

2. Problem statement

The two-phase system domain is depicted schematically in Fig. 1. It consists of a 1D slab containing μ-sized C particles suspended in a CH_4–H_2–Ar gas mixture. The gas–particle flow is directly exposed to an external source of concentrated solar radiation, assumed to have Planck's spectral distribution of a blackbody at 5780 K. Each phase is modeled as a non-uniform and non-gray absorbing–emitting–scattering medium. The boundaries are modeled as black plane walls at $T_{surr} = 0$ K (non-participating surroundings). The composition of each phase and its thermal and optical properties vary with time due to the heterogeneous endothermic reaction occurring at above about 1500 K.

Each particle is assumed isothermal, as justified by the Biot number $\mathrm{Bi} \ll 1$ for the considered size range of the particles. For an opaque particle at temperature T_p suspended in gas flow at $T_g < T_p$, surrounded by cold walls and irradiated by an external flux $\dot{q}_e$, Bi is here defined as the ratio of the internal conduction heat transfer resistance to the external radiation-convection heat transfer resistance,

$$\mathrm{Bi}_r = \frac{d\left\{\varepsilon\left[\frac{\dot{q}_e}{T_p - T_g} - \sigma(T_p + T_g)(T_p^2 + T_g^2)\right] - h\right\}}{k_c}. \tag{1}$$

Each phase is modeled as a quasi-continuous medium using its effective volumetric transport properties [36,37]. The C particles are modeled as absorbing, emitting, and anisotropically scattering, while scattering is neglected for the gas phase. The flow is assumed to be laminar in the direction perpendicular to the boundaries. Radiative and convective heat is exchanged between particles and gas. Mass and heat diffusion are omitted from consideration, thus significantly simplifying the flow analysis [38]. The kinetics of CH_4-decomposition,

$$CH_4 \rightarrow C + 2H_2 \tag{2}$$

was previously modeled for non-solar [39,40] and solar-driven [41,42] reactors. In this study, a simplified first-order Arrhenius-type rate law was applied for a flow of CH_4 laden with μ-sized carbon particles, given by:

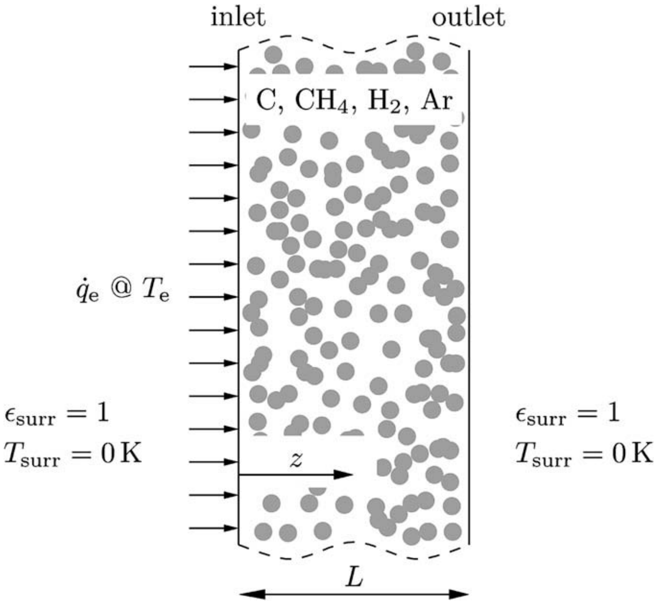

Fig. 1. Scheme of the 1D system domain consisting of a particle–gas mixture exposed to an external source of concentrated solar radiation and undergoing heterogeneous thermochemical reaction.

$$\bar{r} = \bar{\rho}_{\mathrm{C,exp}}^{-1} k_0 \exp\left(-\frac{E_\mathrm{a}}{\bar{R}T}\right)\bar{\rho}_{\mathrm{CH_4}}, \tag{3}$$

where $k_0 = 1.07 \times 10^6\ \mathrm{s}^{-1}$, $\bar{\rho}_{\mathrm{C,exp}} = 8.84\ \mathrm{mol\ m^{-3}}$, and $E_\mathrm{a} = 147\ \mathrm{kJ\ mol^{-1}}$ were determined experimentally in a solar reactor prototype tested under concentrated solar irradiation [42]. This simplified rate law can reasonably describe the reaction rate for the CH$_4$-particle flow conditions existing in the solar reactor (see Section 6), but may not be applied to the catalytic decomposition reaction using other catalysts or to reactors with different mass/heat transfer characteristics. The carbon produced is assumed to deposit on the surface of existing laden particles, resulting in their growth with time and affecting their radiative characteristics. It is assumed that the particle growth does not affect the reaction rate.

3. Radiative heat transfer analysis

Variation of the radiative intensity $I_\lambda(\mathbf{r},\hat{\mathbf{s}})$ along path $\hat{\mathbf{s}}$ in a two-phase medium, where the phases are at thermal non-equilibrium to each other, is described by the equation of radiative transfer in its extended form [37,43],

$$\hat{\mathbf{s}} \cdot \nabla I_\lambda(z,\hat{\mathbf{s}}) = S_\lambda(z,\hat{\mathbf{s}}) - \left[\beta_{\lambda,\mathrm{p}}(z,\hat{\mathbf{s}}) + (1-f_\mathrm{v})\kappa_{\lambda,\mathrm{g}}(z,\hat{\mathbf{s}})\right] I_\lambda(z,\hat{\mathbf{s}}), \tag{4}$$

where $S(z,\hat{\mathbf{s}})$ is the radiative source function,

$$S_\lambda(z,\hat{\mathbf{s}}) = \kappa_{\lambda,\mathrm{p}}(z) I_{\mathrm{b}\lambda}[T_\mathrm{p}(z)] + (1-f_\mathrm{v})\kappa_{\lambda,\mathrm{g}} I_{\mathrm{b}\lambda}[T_\mathrm{g}(z)] + \frac{\sigma_{\mathrm{sca},\lambda,\mathrm{p}}(z)}{4\pi} \times \int_{4\pi} I_\lambda(z,\hat{\mathbf{s}}_\mathrm{i})\Phi_{\lambda,\mathrm{p}}(z,\hat{\mathbf{s}}_\mathrm{i},\hat{\mathbf{s}})\mathrm{d}\Omega_\mathrm{i}, \tag{5}$$

and $\beta_{\lambda,\mathrm{p}}$, $\kappa_{\lambda,\mathrm{p}}$, $\sigma_{\mathrm{sca},\lambda,\mathrm{p}}$ are the spectral extinction, absorption, and scattering coefficients of the solid phase, respectively, $\kappa_{\lambda,\mathrm{g}}$ is the spectral absorption coefficient of the gas phase, and $\Phi_{\lambda,\mathrm{p}}(\hat{\mathbf{s}}_\mathrm{i},\hat{\mathbf{s}})$ is the scattering phase function of the solid phase from $\hat{\mathbf{s}}_\mathrm{i}$ into $\hat{\mathbf{s}}$. The corresponding boundary conditions for Eq. (4) are

- for collimated incident solar flux at $z = 0$,

$$I_\lambda(z=0,\hat{\mathbf{s}}) = \frac{\dot{q}_\mathrm{e}}{\sigma T_\mathrm{e}^4}\pi I_{\lambda\mathrm{b}}(T_\mathrm{p})\delta(\hat{\mathbf{s}}-\hat{\mathbf{k}}) \quad \text{for} \quad \hat{\mathbf{s}}\cdot\hat{\mathbf{k}} > 0, \tag{6}$$

- for diffuse incident solar flux at $z = 0$,

$$I_\lambda(z=0,\hat{\mathbf{s}}) = \frac{\dot{q}_\mathrm{e}}{\sigma T_\mathrm{e}^4}\pi I_{\lambda\mathrm{b}}(T_\mathrm{p}) \quad \text{for} \quad \hat{\mathbf{s}}\cdot\hat{\mathbf{k}} > 0, \tag{7}$$

- for the boundary at $z = L$,

$$I_\lambda(z=L,\hat{\mathbf{s}}) = 0 \quad \text{for} \quad \hat{\mathbf{s}}\cdot\hat{\mathbf{k}} < 0. \tag{8}$$

Radiative properties of C particles are calculated by assuming independent scattering and the refractive index of the gas phase to be equal to unity [44]. The absorption and scattering coefficients are computed by using the monodisperse approximation [43,45],

$$\{\kappa_{\lambda,\mathrm{p}}, \sigma_{\mathrm{sca},\lambda,\mathrm{p}}, \beta_\lambda\} = \pi\int_0^\infty \{Q_{\mathrm{abs},\lambda,\mathrm{p}}, Q_{\mathrm{sca},\lambda,\mathrm{p}}, Q_{\mathrm{ext},\lambda,\mathrm{p}}\} r^2 f(r)\mathrm{d}r \approx \frac{3f_\mathrm{v}}{2d_{32}}\{Q_{\mathrm{abs},\lambda,\mathrm{p}}, Q_{\mathrm{sca},\lambda,\mathrm{p}}, Q_{\mathrm{ext},\lambda,\mathrm{p}}\}. \tag{9}$$

In Eq. (9), $f(r)\mathrm{d}r$ is the number of spherical particles of radius between r and $r + \mathrm{d}r$ per unit volume and d_{32} is the Sauter mean particle diameter [45]. The absorption, scattering, and extinction efficiency factors and the scattering phase function are obtained by applying the Mie theory [46], based on the particle size parameter $\xi = \pi d/\lambda$ in the range 10^{-2}–10^2 and the complex refractive index of the particle $m = n - ik$ approximated by that of propane soot [47,48]. The absorption coefficient of the gas phase $\kappa_{\lambda,\mathrm{g}}$ is computed by applying the line-by-line model to the molecular spectroscopic database HITRAN-2004 for CH$_4$ [49–51], to calculate the high-resolution ($\Delta\eta = \Delta\lambda/\lambda^2 = 9.9\ \mathrm{m}^{-1}$) spectral absorption coefficient $\kappa_{\lambda,\mathrm{g}}^*$ in the wavelength range 10^{-7}–10^{-5} m, which in turn is used to calculate the low-resolution absorption coefficient of the gas mixture by the box model [43],

$$\kappa_{\eta,\mathrm{g}}(p_{\mathrm{CH_4}}, p_0, T_\mathrm{g}) = \frac{1}{\Delta\eta_{\mathrm{box}}}\int_{\Delta\eta_{\mathrm{box}}} \kappa_{\eta,\mathrm{g}}^*(p_{\mathrm{CH_4}}, p_0, T_\mathrm{g})\mathrm{d}\eta. \tag{10}$$

H$_2$ and Ar are assumed to be radiatively non-participating. The pathlength Monte Carlo method with ray redirection is applied to compute radiative flux divergence in the gas and solid phases [52],

$$\frac{\partial \dot{q}_{\mathrm{r,g}}}{\partial z} = \int_0^\infty \frac{(1-f_\mathrm{v})\kappa_{\lambda,\mathrm{g}}}{\kappa_{\lambda,\mathrm{p}} + (1-f_\mathrm{v})\kappa_{\lambda,\mathrm{g}}}\frac{\partial \dot{q}_{\mathrm{r},\lambda}}{\partial z}\mathrm{d}\lambda \approx (1-f_\mathrm{v})\left(4\kappa_{\mathrm{P,g}}\sigma T_\mathrm{g}^4 - \frac{\sum_k \dot{q}_{\mathrm{ray},k}\kappa_{\lambda,\mathrm{g}}\mathrm{d}s_k}{\mathrm{d}z}\right), \tag{11}$$

$$\frac{\partial \dot{q}_{\mathrm{r,p}}}{\partial z} = \int_0^\infty \frac{\kappa_{\lambda,\mathrm{p}}}{\kappa_{\lambda,\mathrm{p}} + (1-f_\mathrm{v})\kappa_{\lambda,\mathrm{g}}}\frac{\partial \dot{q}_{\mathrm{r},\lambda}}{\partial z}\mathrm{d}\lambda \approx 4\kappa_{\mathrm{P,p}}\sigma T_\mathrm{p}^4 - \frac{\sum_k \dot{q}_{\mathrm{ray},k}\kappa_{\lambda,\mathrm{p}}\mathrm{d}s_k}{\mathrm{d}z}, \tag{12}$$

where k designates a generic stochastic ray traversing in 3D the path length $\mathrm{d}s_k$ within sub-layer of thickness $\mathrm{d}z$ and carrying a portion of radiative flux $\dot{q}_{\mathrm{ray},k} = \left(\dot{q}_\mathrm{e} + 4\sigma\int_0^L\left(\kappa_{\mathrm{P,g}}T_\mathrm{g}^4 + \kappa_{\mathrm{P,p}}T_\mathrm{p}^4\right)\mathrm{d}z\right)N_{\mathrm{rays}}^{-1}$. The path length to a scattering event is

$$\ln \mathscr{R}_s = -\int_0^s \sigma_{\mathrm{sca},\lambda,\mathrm{p}}(s)\mathrm{d}s, \tag{13}$$

where $\mathscr{R}_s$ is a random number chosen from a uniform distribution set between 0 and 1. The corresponding probabilistic cumulative distribution functions for the wavelength and direction of emission of each phase, and direction of scattering by particles are equivalent to those employed in the classic collision-based MC for two-phase media [53].

4. Mass and energy conservation equations

4.1. Mass conservation

Transient 1D mass conservation equations are formulated separately for the solid and the gas phases. The molar concentration and molar flux of the gas component i (i = CH$_4$, H$_2$, Ar) are obtained from:

$$\frac{\partial\bar{\rho}_g}{\partial t} = -\frac{\partial\dot{n}_g}{\partial z} + \bar{\rho}_p\bar{r}\sum_i \nu_i, \qquad \bar{\rho}_g(t, 0 \leqslant z \leqslant L) = \frac{(1-f_v)p_0}{\bar{R}T_g}, \quad \dot{n}_g(t \geqslant 0, z=0) = \dot{n}_{g,0}, \tag{14}$$

$$\frac{\partial(\bar{\rho}_g\bar{x}_i)}{\partial t} = -\frac{\partial(\dot{n}_g\bar{x}_i)}{\partial z} + \bar{\rho}_p\nu_i\bar{r}, \qquad \sum_i \bar{x}_i = 1, \quad \bar{x}_i(t=0, 0 \leqslant z \leqslant L) = \bar{x}_i(t \geqslant 0, z=0) = \bar{x}_{i,0}, \tag{15}$$

where ν_i is the stoichiometric coefficient of the gas component i in reaction (2); $\nu_{CH_4} = -1$, $\nu_{H_2} = 2$, and $\nu_{Ar} = 0$. The molar concentration of carbon and the number of particles are obtained from:

$$\frac{\partial\bar{\rho}_p}{\partial t} = -\frac{\partial\dot{n}_p}{\partial z} + \bar{\rho}_p\nu_C\bar{r}, \quad \bar{\rho}_p = \frac{\rho_C f_v}{\bar{M}_C}, \quad \dot{n}_p(t \geqslant 0, z=0) = \dot{n}_{p,0}, \tag{16}$$

$$\frac{\partial\Gamma_p}{\partial t} = -\frac{\partial\dot{\gamma}_p}{\partial z}, \quad \dot{\gamma}_p = \frac{6\bar{M}_C\dot{n}_p}{\rho_C\pi d^3}, \quad \Gamma = \frac{6f_v}{\pi d^3}, \tag{17}$$

$$f_v(t=0, 0 \leqslant z \leqslant L) = f_v(t \geqslant 0, z=0) = f_{v,0}, \quad d(t=0, 0 \leqslant z \leqslant L) = d(t \geqslant 0, z=0) = d_0, \tag{18}$$

where $f_{v,0}$ and d_0 are the inlet and initial particle volume fraction and diameter, respectively. The particle density of carbon is taken as $\rho_C = 2270$ kg m^{-3}. Furthermore, the carbon molar flux and mean particle diameter satisfy the following conditions,

$$\dot{n}_p = \begin{cases} \dot{n}_{p,0} & \text{for} \quad z = 0, \\ \frac{\partial\bar{\rho}_p}{\partial\bar{\rho}_g}\dot{n}_g & \text{for} \quad z > 0, \end{cases} \tag{19}$$

$$d = \begin{cases} d_0 & \text{for} \quad t = 0, \\ \left(\frac{6f_v}{\pi\Gamma}\right)^{\frac{1}{3}} & \text{for} \quad t > 0, \end{cases} \tag{20}$$

where the particles are assumed to be suspended in the flow, thus no relative movement between gas and particles is considered. Eqs. (14)–(18) are derived by assuming no accumulation of gaseous components, no creation of new particles, and negligible effect of the gas volume change due to the particle growth.

4.2. Energy conservation

Transient 1D energy conservation equations are formulated separately for the solid and gas phases. For the gas phase at constant pressure,

$$\bar{c}_{p,g}\bar{\rho}_g\frac{\partial T_g}{\partial t} = -\bar{c}_{p,g}\dot{n}_g\frac{\partial T_g}{\partial z} - \frac{\partial\dot{q}_{r,g}}{\partial z} + \Gamma\pi d^2 h(T_p - T_g) + \bar{\rho}_p\nu_{H_2}\bar{r}\left[\bar{h}_{H_2}(T_p) - \bar{h}_{H_2}(T_g)\right], \tag{21}$$

$$T_g(t=0, 0 \leqslant z \leqslant L) = T_g(t \geqslant 0, z=0) = T_{g,0}. \tag{22}$$

For the solid phase,

$$\bar{c}_{p,p}\bar{\rho}_p\frac{\partial T_p}{\partial t} = -\bar{c}_{p,p}\dot{n}_p\frac{\partial T_p}{\partial z} - \frac{\partial\dot{q}_{r,p}}{\partial z} - \Gamma\pi d^2 h(T_p - T_g) - \bar{\rho}_p\bar{r}\left(\sum_i \nu_i\bar{h}_i + \bar{h}_C\right), \tag{23}$$

$$T_p(t=0, 0 \leqslant z \leqslant L) = T_p(t \geqslant 0, z=0) = T_{p,0}, \tag{24}$$

where $\bar{h}_{CH_4} = \bar{h}_{CH_4}(T_g)$, $\bar{h}_{H_2} = \bar{h}_{H_2}(T_p)$, and $\bar{h}_C = \bar{h}_C(T_p)$. The limiting sphere model [35] is employed to compute the partial heat transfer coefficient h_i between a particle and gaseous component i. The overall heat transfer coefficient is then $h = x_i h_i$, assuming independence from the inter-phase mass transfer and cross-interactions between molecules of different gaseous components.

The finite volume method is applied to discretize Eqs. (11)–(24) in space [38,54,55]. Time integration is performed by applying the explicit Euler scheme [38,54,55]. Note that MC needs to be run at each time step due to time-variation of the radiative characteristics of each phase as the chemical reaction progresses.

5. Numerical results

The baseline simulation parameters are summarized in Table 1 and are used in all simulation runs unless stated otherwise. Absorption and extinction efficiency factors of C particles are plotted in Fig. 2 as a function of radiation wavelength for selected particle diameters d = 1, 2.5, 5, and 10 μm. As expected for geometric optics, $Q_{ext,\lambda,p}$ approaches the value of 2 and $Q_{abs,\lambda,p}$ the value of 1 for short wavelengths. Thus, refraction and reflection at short wavelengths is negligible while scattering is due to diffraction. Fig. 3 shows the scattering phase functions for two particle diameters, d = 1 and 10 μm, and two radiation wavelengths λ = 0.5 and 2 μm, corresponding to the peak for solar radiation and for Planck's emissive power at 1450 K (above which CH$_4$-decomposition proceeds at reasonable rates), respectively. For d = 10 μm, the forward

Table 1
Baseline parameters.

Parameter	Value	Unit
L	0.1	m
$L/\Delta z$	50	–
N_{rays}	10^6	–
p_0	101,325	Pa
$\dot{q}_e$	1.5×10^6	W m^{-2}
T_e	5780	K
$T_{g,0}$	300	K
$T_{p,0}$	300	K
T_{surr}	0	K
ε_{surr}	1	–

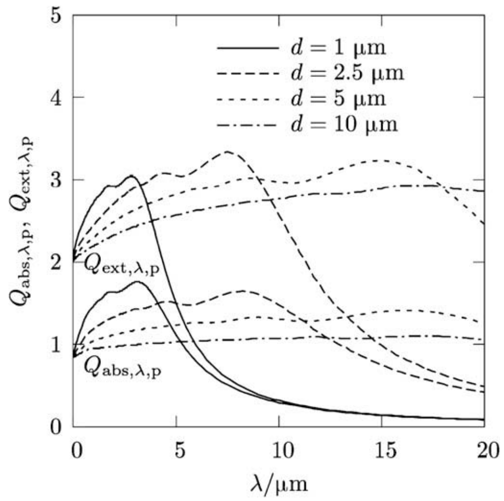

Fig. 2. Spectral extinction and absorption efficiency factors of carbon particles for selected particle diameters d = 1, 2.5, 5, and 10 μm.

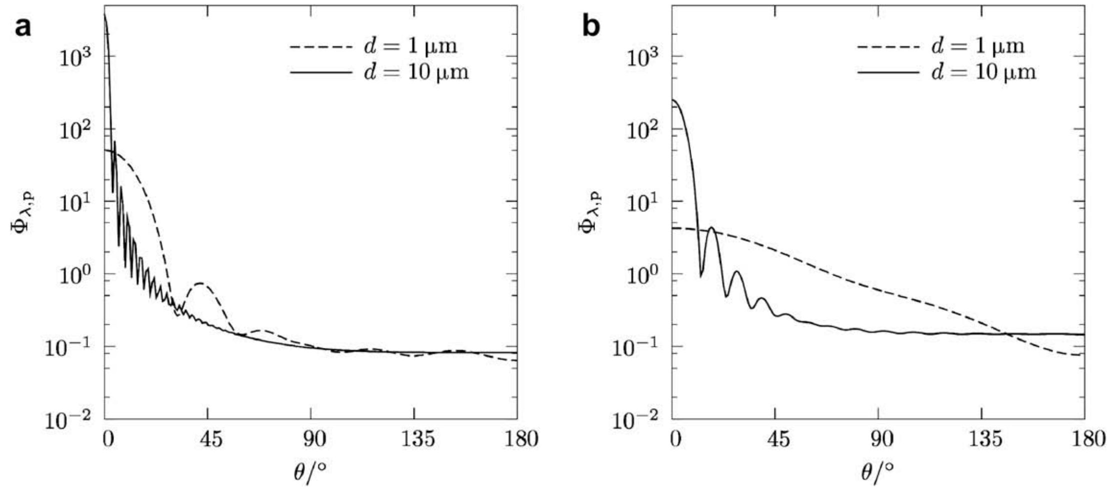

Fig. 3. Scattering phase function of the particles for selected particle diameters $d = 1$ and 10 µm, and at radiation wavelength of (a) $\lambda = 0.5$ µm and (b) $\lambda = 2$ µm.

scattering is highly predominant at both wavelengths, but this effect diminishes for $d = 1$ µm particles, especially at $\lambda = 2$ µm. Temperature response of the C particles at $z = L/2$ is shown in Fig. 4 for selected initial and inlet particle diameters $d_0 = 1$, 2.5, 5, and 10 µm. Both the heating rate and the steady-state temperature increase with decreasing particle size. For $d_0 = 1$ µm, 1500 K is reached in approximately 0.1 s, and steady-state temperature of 1740 K is reached in less than 0.2 s, demonstrating the capability of extreme heating rates in directly-irradiated solar reactors. Even for $d_0 = 10$ µm, steady state is still attained in less than 0.6 s. Higher temperatures and heating rates with smaller particles are due to augmented extinction of incident solar radiation, both by absorption and scattering, and due to the lower values of the "cut-off" wavelength that limit the particles' ability to emit radiation (see also Fig. 3).

Fig. 5 shows the variation of the spectral absorption and extinction coefficients with time at $z = L/2$ for $f_{v,0} = 10^{-5}$ and $\lambda = 0.5$ µm, and for two initial particle diameters $d_0 = 1$ and 10 µm. The initial $\kappa_{\lambda,p}$ for $d_0 = 1$ µm is larger by one order of magnitude than that for $d_0 = 10$ µm. The rapid decrease of both $\kappa_{\lambda,p}$ and $\beta_{\lambda,p}$ in the initial 150 ms is explained by the decrease of f_v as a result of gas thermal expansion during the rapid heating phase. This effect is more pronounced for smaller particles as they reach higher steady-state temperatures. Thereafter, the radiation coefficients undergo a slight but steady increase because of increasing f_v caused by particle growth during CH_4-decomposition. The latter effect cannot be observed for the larger 10 µm-particles because of their lower steady-state temperatures, as observed in Fig. 3, and hence a significantly lower rate of CH_4-decomposition and particle growth.

Fig. 6 shows the cumulative fraction of the incident solar radiation being absorbed directly or after single or multiple scattering along the slab at steady state for $d_0 = 1$, 2.5, 5, and 10 µm. It is defined as:

$$A(z) = \frac{\int_0^z \frac{\partial \dot{q}_{\mathrm{abs}}}{\partial z^*} dz^*}{\dot{q}_{\mathrm{e}}}. \tag{25}$$

The total amount of absorbed solar radiation increases dramatically when the initial particle size is reduced: from about 12% for $d_0 = 10$ µm to over 65% for $d_0 = 1$ µm.

Figs. 7–9 show the variation of the steady-state temperature profiles across the slab with particle diameter (Fig. 7), particle volume fraction (Fig. 8), and CH_4 molar concentration (Fig. 9). Increasing $f_{v,0}$ at constant d_0 or decreasing d_0 at constant $f_{v,0}$ leads to elevated steady-state temperatures as compared to those for the baseline case because of higher $\kappa_{\lambda,p}$ and $\beta_{\lambda,p}$, and consequently

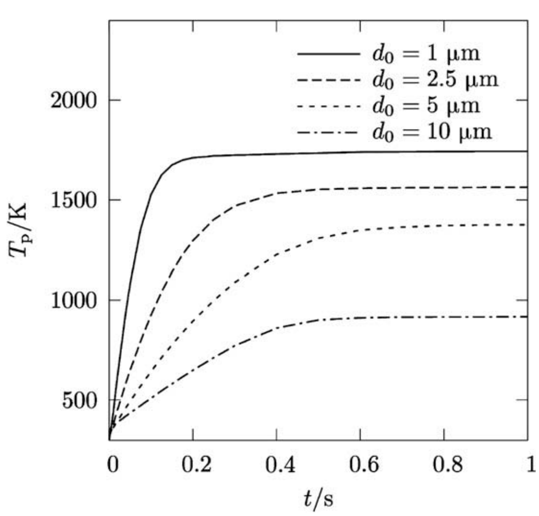

Fig. 4. Transient particle temperature at $z = L/2$ as a function of time for selected inlet/initial particle diameters $d_0 = 1$, 2.5, 5, and 10 µm.

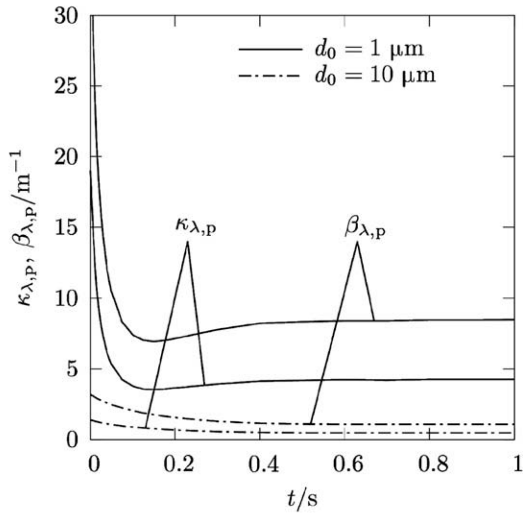

Fig. 5. Transient spectral absorption and extinction coefficients at $z = L/2$ for $f_{v,0} = 10^{-5}$, $\lambda = 0.5$ µm, and for inlet/initial particle diameters $d_0 = 1$ and 10 µm.

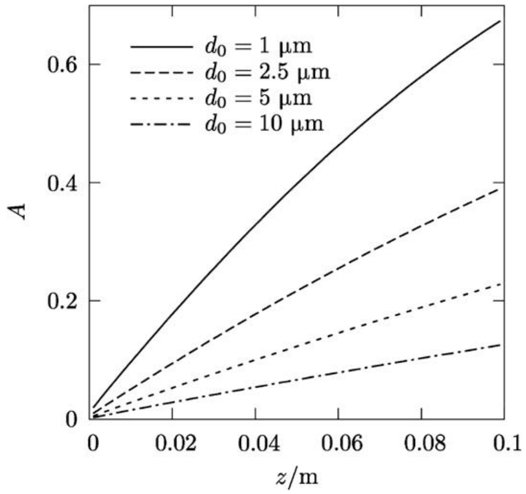

Fig. 6. Steady-state cumulative absorbed fraction of external radiation along the slab for selected inlet/initial particle diameters $d_0 = 1$, 2.5, 5, and 10 μm.

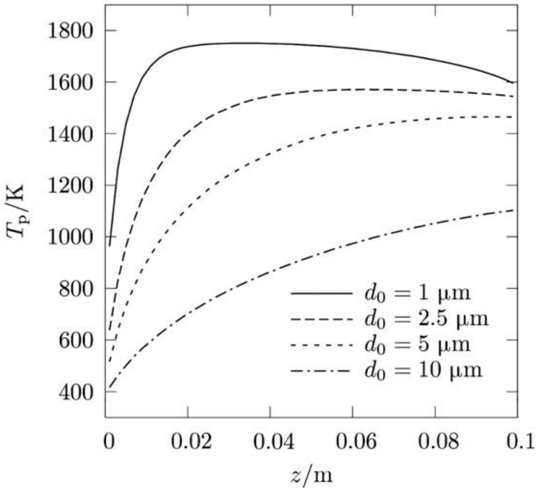

Fig. 7. Steady-state particle temperature profile along the slab for selected inlet/initial particle diameters $d_0 = 1$, 2.5, 5, and 10 μm.

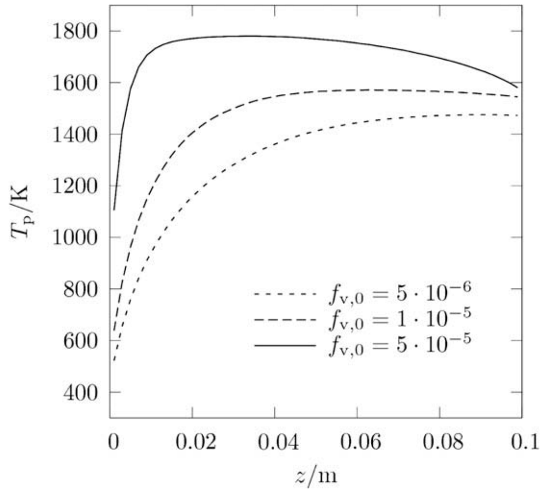

Fig. 8. Steady-state particle temperature profile for selected inlet/initial particle volume fractions $f_{v,0} = 0.5 \times 10^{-5}$, 1×10^{-5}, and 5×10^{-5}.

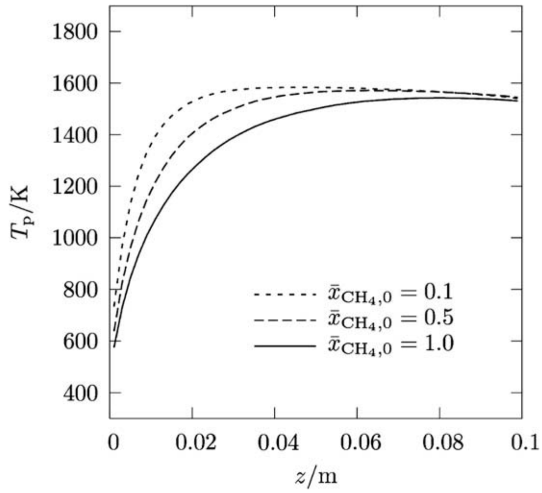

Fig. 9. Steady-state particle temperature profile for selected inlet/initial methane molar fractions $\bar{x}_{CH_4,0} = 0.1, 0.5$, and 1.

effective extinction. In contrast, an increase in CH_4 concentration lowers the temperatures of both phases in spite of increasing $\kappa_{\lambda,g}$ as a result of the 2–5 times higher $\bar{c}_p$ of CH_4 than that of Ar in the relevant temperature range.

The computations revealed that for the range of particle sizes, volume fractions, and methane molar fractions considered, the difference between the particle and gas temperatures at steady state is insignificant and reached a maximum of 53 K for $d_0 = 10$ μm, $f_{v,0} = 10^{-5}$, $\bar{x}_{CH_4,0} = 0.5$, and $z/L = 0.01$. External thermal radiation is predominantly absorbed by the particles. For example, in the latter case, particles absorb about 100 times more effectively than the gas. Heat transfer between the solid and gas phases is predominantly by convection and by gas IR emission.

6. Experimental

The engineering design and fabrication of a 5 kW particle-flow solar reactor prototype has been described previously in detail [56]: only the main features are summarized here. Fig. 10 depicts its configuration. It consists of a 200 mm-height 100 mm-diameter cylindrical cavity-receiver, made of 10 mm-thick steel alloy, containing a 60 mm-diameter circular aperture. A 240 mm-diameter 3-mm thick quartz window is mounted 80 mm in front of the

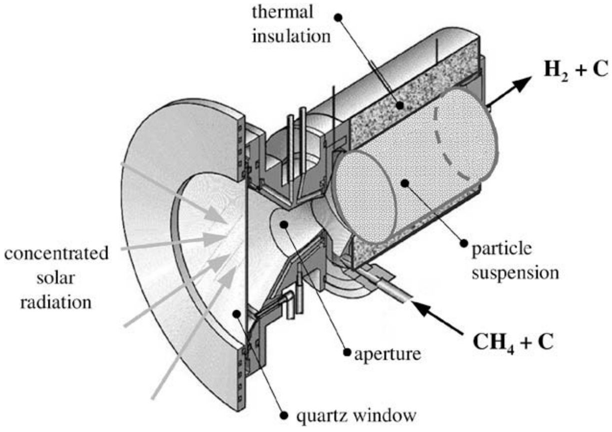

Fig. 10. Schematic of the solar reactor prototype, featuring a flow of CH_4 laden with C particles and directly exposed to concentrated solar radiation.

aperture on a water-cooled conical copper funnel. Cooling and purging of the window is accomplished by Ar injected through four nozzles at the front cone. CH_4 – pure or diluted with Ar – and laden with carbon particles is injected through four inlet nozzles, located 30 mm behind the aperture, into the high radiative flux zone where the particles are instantaneously heated to 1300–1500 K. The gas–particle flow progresses towards the rear part of the reactor as the reaction occurs. The products exiting the reactor were cooled and filtered downstream. Experimentation was performed at ETH's High-Flux Solar Simulator [57]: a high-pressure Ar arc close-coupled with a high precision elliptical trough reflector, to provide an external source of intense thermal radiation that approaches the heat transfer characteristics of highly concentrating solar systems. Incoming radiative flux at the focal plane was measured optically by a calibrated CCD camera focused on a water-cooled Al_2O_3-plasma-coated Lambertian target, and integrated over the aperture to yield the radiative power input, with an accuracy of $\pm^{9}_{13}\%$. The mean radiative flux $\dot{q}_e$ was obtained by dividing it by the aperture area. The mass flow rates were controlled using Bronkhorst HI-TEC electronic flow controllers. The gaseous products were analyzed on-line by gas chromatography (GC, Agilent High Speed Micro G2890A; 10 ppm detection limit; sampling rate 0.01 Hz), supplemented by IR-based detectors for CH_4, CO, and CO_2 (Siemens Ultramat 23; 0.2% detection limit; sampling rate 1 Hz), and a thermal-conductivity-based detector for H_2 (Siemens Calomat 6; 50 ppm detection limit; sampling rate 1 Hz). A known constant flow of N_2 is injected into the exhaust line before the gas analysis as calibration gas.

The reaction extent is defined as:

$$X_{CH_4} = 1 - \frac{\bar{x}_{CH_4}(t \to \infty, z = z_{outlet})}{\bar{x}_{CH_4,0}}. \tag{26}$$

Fig. 11a and b shows the numerically computed and experimentally measured temperatures and reaction extents, respectively, as a function of the external radiative flux $\dot{q}_e$ in the range 664–869 kW m^{-2} and for fixed $f_v = 9.2 \times 10^{-5}$, $\dot{V}_g = 16.8\ l_N min^{-1}$, and $\bar{x}_{CH_4} = 0.143$. Fluka 05100 active carbon particles of $d_{32} = 23\ \mu m$ were laden in the CH_4 flow. The measured temperature, shown in Fig. 11a, is the average of three type-K thermocouples located at the inner reactor wall at $z = 4$ cm. The error bars correspond to the maximum difference between the 3 values. The computed temperature is taken for the gas phase and averaged over 2 cm < z < 6 cm. The temperature increased from 1194 K for $\dot{q}_e = 664$ kW m^{-2} to 1306 K for $\dot{q}_e = 869$ kW m^{-2}. This increase is the natural response of the reacting system to a higher absolute amount of absorbed radiation to reach thermal equilibrium, which in turn leads to an increase of the chemical reaction extent. As indicated in Fig. 6, a considerable part of the incident external radiation is lost by transmission, directly or after single or multiple scattering. The cavity effect augmented radiation absorption by internal multiple reflections on the reactor inner walls, but relatively high heat losses were observed experimentally through the front part of the cavity that was in direct contact with the water-cooled frontal copper funnel.

Fig. 11b shows the measured and simulated extent of the chemical reaction for two cases: (1) using E_a and k_0 from [42], and (2) using fitted E_a and k_0. Considering the reasonable good temperature agreement shown in Fig. 11a, as well as the relatively low contribution of the chemical reaction to the energy balance (<1% of $\dot{q}_e$ is used to drive the endothermic reaction in these experimental runs), the difference between the computed and measured X_{CH_4} is attributed to the selected values of E_a and k_0. In case 1, a weaker dependence on $\dot{q}_e$ is obtained for the numerically computed X_{CH_4} leading to an overprediction of X_{CH_4} for $\dot{q}_e < 720$ kW m^{-2}. In case 2, the simulations were performed for $E_a = 260$ kJ mol^{-1} and $k_0 = 1.35 \cdot 10^{10}$ s^{-1}, obtained by fitting the computed and measured X_{CH_4}. The increase in the values of the kinetic parameters is attributed to the effect of particle morphology variations as the chemical reaction progresses.

The maximum measured and calculated reaction extents were 24% and 22%, respectively, both for $\dot{q}_e = 869$ kW m^{-2}. The uncertainties in the measured X_{CH_4} are mainly due to the error of the inlet gas flow controllers. The measured X_{CH_4} exceeds the computed one for $\dot{q}_e < 750$ kW m^{-2} and the opposite is true for $\dot{q}_e < 750$ kW m^{-2}. The relative difference between the computed and measured reaction extent, defined as $|X_{CH_4,num} - X_{CH_4,exp}|/X_{CH_4,num}$, is maximum at 55% for $\dot{q}_e = 664$ kW m^{-2} and minimum at 5% for $\dot{q}_e = 763$ kW m^{-2}.

7. Summary and conclusions

A numerical model has been developed to compute temperature and chemical composition of a reacting two-phase solid–gas flow initially composed of CH_4 laden with carbon particles, and directly exposed to concentrated solar radiation. Maximum (steady-state) temperatures in the range of 1700–1800 K were obtained for initial carbon particles of 1–10 μm diameter and initial volume

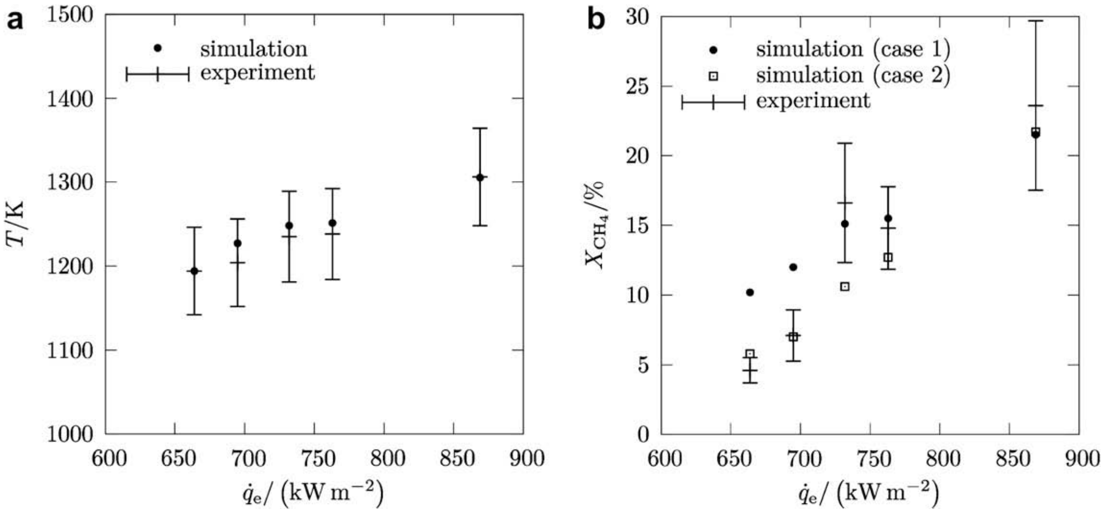

Fig. 11. Comparison between numerically computed (cases1 and 2) and experimentally measured temperatures (a) and reaction extents X_{CH_4} (b). Case 1: using E_a and k_0 from [42]; case 2: using fitted E_a and k_0.

fraction in the range 5×10^{-6}–5×10^{-5}. The maximum CH_4 conversion in steady-state was 46.5% for the inlet and initial volume fraction and particle diameter of $f_{v,0} = 5 \times 10^{-5}$ and $d_0 = 2.5$ μm, corresponding to maximum particle temperatures of 1780 K. Validation was accomplished by comparing the computed steady-state temperatures and reaction extents with those obtained experimentally using a particle-flow solar reactor prototype subjected to concentrated solar radiation.

Acknowledgments

This work has been carried out in the framework of the SOLHYCARB EU-Project, funded by the European Commission under Contract No. SESCT2006-19770.

References

[1] A. Steinfeld, Solar thermochemical production of hydrogen – a review, Sol. Energy 78 (2005) 603–615.
[2] E.A. Fletcher, Solarthermal processing: a review, J. Sol. Energy Eng. 123 (2001) 63–74.
[3] T. Kodama, High-temperature solar chemistry for converting solar heat to chemical fuels, Prog. Energy Combust. Sci. 29 (2003) 567–597.
[4] P. v. Zedtwitz, A. Steinfeld, The solar thermal gasification of coal – energy conversion efficiency and CO_2 mitigation potential, Energy 28 (2003) 441–456.
[5] J. Lédé, Solar thermochemical conversion of biomass, Sol. Energy 65 (1999) 3–13.
[6] J. Matsunami, S. Yoshida, O. Yokota, M. Nezuka, M. Tsuji, Y. Tamaura, Gasification of waste tyre and plastic (pet) by solar thermochemical process for solar energy utilization, Sol. Energy 65 (1999) 21–23.
[7] D. Hirsch, M. Epstein, A. Steinfeld, The solar thermal decarbonization of natural gas, Int. J. Hydrogen Energy 26 (2001) 1023–1033.
[8] S. Abanades, G. Flamant, Solar hydrogen production from the thermal splitting of methane in a high-temperature solar chemical reactor, Sol. Energy 80 (2006) 1321–1332.
[9] S. Abanades, G. Flamant, Hydrogen production from solar thermal dissociation of methane in a high-temperature fluid-wall chemical reactor, Chem. Eng. Process. 47 (2008) 490–498.
[10] J.K. Dahl, A.A.W. Weimer, A. Lewandowski, C. Bingham, F. Bruetsch, A. Steinfeld, Dry reforming of methane using a solar-thermal aerosol flow reactor, Ind. Eng. Chem. Res. 43 (2004) 5489–5495.
[11] A. Wörner, R. Tamme, CO_2 reforming of methane in a solar driven volumetric receiver–reactor, Catal. Today 46 (1998) 165–174.
[12] T. Kodama, T. Shimizu, M. Satoh, M. Nakata, K.-I. Shimizu, Stepwise production of CO-rich syngas and hydrogen via solar methane reforming by using a Ni(II)–ferrite redox system, Sol. Energy 73 (2002) 363–374.
[13] A. Steinfeld, P. Kuhn, A. Reller, R. Palumbo, J. Murray, Y. Tamaura, Solar-processed metals as clean energy carriers and water-splitters, Int. J. Hydrogen Energy 23 (9) (1998) 767–774.
[14] M. Halmann, A. Frei, A. Steinfeld, Carbothermal reduction of alumina: thermochemical equilibrium calculations and experimental investigation, Energy 32 (2007) 2420–2427.
[15] R. Palumbo, M. Keunecke, S. Möller, A. Steinfeld, Reflections on the design of solar thermal chemical reactors: thoughts in transformation, Energy 29 (2004) 727–744.
[16] W. Lipiński, A. Steinfeld, Transient radiative heat transfer within a suspension of coal particles undergoing steam gasification, Heat Mass Transfer 41 (2005) 1021–1032.
[17] W. Lipiński, A. Z'Graggen, A. Steinfeld, Transient radiation heat transfer within a nongray nonisothermal absorbing–emitting–scattering suspension of reacting particles undergoing shrinking, Numer. Heat Transfer B 47 (2005) 443–457.
[18] W. Lipiński, A. Steinfeld, Heterogeneous thermochemical decomposition under direct irradiation, Int. J. Heat Mass Transfer 47 (2004) 1907–1916.
[19] R. Müller, W. Lipiński, A. Steinfeld, Transient heat transfer in a directly-irradiated solar chemical reactor for the thermal dissociation of ZnO, Appl. Therm. Eng. 28 (2008) 524–531.
[20] L. Dombrovsky, L. Schunk, W. Lipiński, A. Steinfeld, An ablation model for the thermal decomposition of porous zinc oxide layer heated by concentrated solar radiation, Int. J. Heat Mass Transfer 52 (11–12) (2009) 2444–2452.
[21] T. Osinga, G. Olalde, A. Steinfeld, Solar carbothermal reduction of ZnO: shrinking packed-bed reactor modeling and experimental validation, Ind. Eng. Chem. Res. 43 (2004) 7981–7988.
[22] D. Hirsch, A. Steinfeld, Radiative transfer in a solar chemical reactor for the co-production of hydrogen and carbon by thermal decomposition of methane, Chem. Eng. Sci. 59 (2004) 5771–5778.
[23] S. Kräupl, A. Steinfeld, Monte Carlo radiative transfer modeling of a solar chemical reactor for the co-production of zinc and syngas, J. Sol. Energy Eng. 127 (2005) 102–108.
[24] P. v. Zedtwitz, W. Lipiński, A. Steinfeld, Numerical and experimental study of the gas–particle radiative exchange for the steam-gasification of coal in a directly-irradiated fluidized bed, Chem. Eng. Sci. 62 (2007) 599–607.
[25] A. Belghit, M. Daguenet, A. Reddy, Heat and mass transfer in a high temperature packed moving bed subjected to an external radiative source, Chem. Eng. Sci. 55 (2000) 3967–3978.
[26] A. Z'Graggen, A. Steinfeld, A two-phase reactor model for the steam-gasification of carbonaceous materials under concentrated thermal radiation, Chem. Eng. Process. 47 (4) (2008) 655–662.
[27] A. Belghit, S. El Issami, Hydrogen production by steam gasification of coal in gas–solid moving bed using nuclear heat, Energy Convers. Manage. 42 (2001) 81–99.
[28] D.P. Ross, H.-M. Yan, Z. Zhong, D.-K. Zhang, A non-isothermal model of a bubbling fluidized-bed coal gasifier, Fuel 84 (2005) 1469–1481.
[29] H. Watanbe, M. Otaka, Numerical simulation of coal gasification in entrained flow coal gasifier, Fuel 85 (2006) 1935–1943.
[30] S.C. Mishra, M. Steven, S. Nemoda, P. Talukdar, D. Trimis, F. Durst, Heat transfer analysis of a two-dimensional rectangular porous radiant burner, Int. Commun. Heat Mass Transfer 33 (2005) 467–474.
[31] T.W. Tong, M.M. Abou-Ellail, Y. Li, A discrete ordinate thermal radiation model for reacting flows in porous burners, in: D. Lemonnier, N. Selçuk, P. Lybaert (Eds.), Eurotherm Seminar 78 on Computational Thermal Radiation in Participating Media II, Poitiers, 2006, pp. 379–388.
[32] C. di Blasi, Heat, momentum and mass transport through a shrinking biomass particle exposed to thermal radiation, Chem. Eng. Sci. 51 (1996) 1121–1132.
[33] M. Abdelrahman, P. Fumeaux, P. Suter, Study of solid–gas suspensions used for direct absorption of concentrated solar radiation, Sol. Energy 22 (1979) 45–48.
[34] G. Evans, H. Houf, R. Greif, C. Crowe, Gas–particle flow within a high-temperature solar cavity receiver including radiation heat transfer, J. Sol. Energy Eng. 109 (1987) 134–142.
[35] H.H. Klein, J. Karni, R. Ben-Zvi, R. Bertocchi, Heat transfer in a directly irradiated solar receiver/reactor for solid–gas reactions, Sol. Energy 81 (2007) 1227–1239.
[36] M. Kaviany, Principles of Heat Transfer in Porous Media, second ed., Springer, New York, 1995.
[37] K.S. Adzerikho, E.F. Nogotov, V.P. Trofimov, Radiative Heat Transfer in Two-Phase Media, CRC Press, Boca Raton, FL, 1993.
[38] S.V. Patankar, Numerical Heat Transfer and Fluid Flow, Hemisphere Publishing Corporation, New York, 1980.
[39] M.H. Kim, E.K. Lee, J.H. Jun, S.J. Kong, G.Y. Han, B.K. Lee, T.-J. Lee, K.J. Yoon, Hydrogen production by catalytic decomposition of methane over activated carbons: kinetic study, Int. J. Hydrogen Energy 29 (2004) 187–193.
[40] N. Muradov, Z. Chen, F. Smith, Fossil hydrogen with reduced CO_2 emission: modeling thermocatalytic decomposition of methane in a fluidized bed of carbon particles, Int. J. Hydrogen Energy 30 (2005) 1149–1158.
[41] S. Rodat, S. Abanades, J. Coulié, G. Flamant, Kinetic modelling of methane decomposition in a tubular solar reactor, Chem. Eng. J. 146 (2009) 120–127.
[42] D. Trommer, D. Hirsch, A. Steinfeld, Kinetic investigation of the thermal decomposition of CH_4 by direct irradiation of a vortex flow laden with carbon particles, Int. J. Hydrogen Energy 29 (2004) 627–633.
[43] M.F. Modest, Radiative Heat Transfer, second ed., Academic Press, New York, 2003.
[44] C.L. Tien, B.L. Drohlen, Thermal radiation in particulate media with dependent and independent scattering, Annu. Rev. Numer. Fluid Mech. Heat Transfer 1 (1987) 1–32.
[45] L.A. Dombrovsky, Radiation Heat Transfer in Disperse Systems, Begell House, New York, 1996.
[46] C.F. Bohren, D.R. Huffman, Absorption and Scattering of Light by Small Particles, Wiley, New York, 1983.
[47] W.H. Dalzell, A.F. Sarofim, Optical constants of soot and their application to heat flux calculations, J. Heat Transfer 91 (1969) 614–618.
[48] T.C. Bond, R.W. Bergstrom, Light absorption by carbonaceous particles: an investigative review, Aerosol Sci. Technol. 40 (2006) 27–67.
[49] J. Taine, A. Soufiani, Gas IR radiative properties: from spectroscopic data to approximate models, in: J.P. Harnett, T.F. Irvine (Eds.), Advances in Heat Transfer, vol. 33, Academic Press, San Diego, 1999, pp. 295–414.
[50] L.S. Rothman et al., The HITRAN molecular spectroscopic database and HAWKS (HITRAN Atmospheric Workstation): 1996 Edition, J. Quant. Spectrosc. Radiat. Transfer 60 (1998) 665–710.
[51] L.S. Rothman et al., The HITRAN-2004 molecular spectroscopic database, J. Quant. Spectrosc. Radiat. Transfer 96 (2005) 139–204.
[52] J.T. Farmer, J.R. Howell, Comparison of Monte Carlo strategies for radiative transfer in participating media, in: J.P. Harnett, T.F. Irvine (Eds.), Advances in Heat Transfer, vol. 31, Academic Press, San Diego, 1998, pp. 333–429.
[53] W.-J. Yang, H. Taniguchi, K. Kudo, Radiative heat transfer by the Monte Carlo method, in: J.P. Harnett, T.F. Irvine (Eds.), Advances in Heat Transfer, vol. 27, Academic Press, San Diego, 1995, pp. 3–215.
[54] C. Hirsch, Numerical computation of internal and external flows, Fundamentals of Numerical Discretization, vol. 1, Wiley, Chichester, 1997.
[55] J.H. Ferziger, M. Perić, Computational Methods for Fluid Dynamics, Springer, Berlin, 2002.
[56] D. Hirsch, A. Steinfeld, Solar hydrogen production by thermal decomposition of natural gas using a vortex-flow reactor, Int. J. Hydrogen Energy 29 (2004) 47–55.
[57] D. Hirsch, P. von Zedtwitz, T. Osinga, J. Kinamore, A. Steinfeld, A new 75 kW high-flux solar simulator for high-temperature thermal and thermochemical research, J. Sol. Energy Eng. 125 (2003) 117–120.